scientific data

OPEN

DATA DESCRIPTOR

Trajectories of a magnetic sphere in a shaken three-dimensional granular bed under low gravity

Ke Cheng[1,2], Meiying Hou[1]✉, Wei Sun[3], Zhihong Qiao[3], Xiang Li[3], Tuo Li[1] & Mingcheng Yang[1,4,5]

This present investigation employs an advanced magnetic particle tracking method to trace the trajectories of an intruder within a vibration-driven granular medium under artificial low-gravity conditions. The experiments are carried out within the centrifuge of the Chinese Space Station, encompassing six distinct low-gravity environments. Trajectories under various vibration modes are captured and analysed for each gravity level. This paper offers an exhaustive account of data collection and algorithms used for data processing, ensuring the dependability and precision of the datasets obtained. Additionally, we make the raw magnetic field data, processing scripts, and visualization tools accessible to the public. This research contributes a comprehensive dataset that is instrumental in exploring the mechanisms of granular segregation under low gravity and aids in the verification of novel physical models for understanding intruder dynamics in granular systems under such conditions.

Background & Summary

Granular matter is ubiquitous on Earth and in space. With the increasing frequency of human deep space exploration activities, the detection of lunar regolith composition by small satellite impacts, and the landing and traversal of rovers, it is essential to investigate and gain a deeper understanding of the penetration dynamics of intruder in low-gravity granular media[1–4]. Besides, the ballistic sorting effect[5,6] and Brazil nut effect (BNE)[7–12], are found playing a possible role in shaping the surface features of small celestial bodies[13–16], such as the formation of craters and the distribution of large boulders[17,18] on the surface of asteroid. Understanding the intruder dynamics in microgravity[19] and low gravity[13–16] is crucial in providing insights into the mechanism of BNE on microgravity celestial bodies and the formation and evolution of planetesimals.

The motion of an intruder within a shaken granular bed can be complicated. It may move either upward or downward when the bed is disturbed. The complexity arises from the interplay of various mechanisms, including convection[8,11,20–26], void-filling[9,27–29], buoyancy[30–34], and inertia[31,35]. Buoyancy predominates at high-frequency vibrations, whereas inertia or convection is more significant at lower frequencies[31]. Under strong vibrations, the reverse Brazil nut effect (RBNE) occurs, causing larger particles to settle at the bottom[36–40]. The upward movement velocity of an intruder within a granular bed under the reduced gravitational conditions of Mars and the Moon was measured in a parabolic flight experiment[41] and was replicated by simulation studies[14–16]. A scaling relationship was identified, demonstrating that the intruder's upward velocity is proportional to the square root of gravity.

However, previous experimental studies on the BNE primarily focused on observing the initial and final states of the intruder, lacking a detailed dynamical analysis of the intermediate processes. Experiments conducted during parabolic flights also faced limitations since parabolic flights could not provide prolonged and stable gravity, and thus only few gravity levels were tested. Centrifuge aboard the Space Station can overcome this shortage and provide a platform for systematic investigations in various reduced gravities. Furthermore, advancements in magnetic particle tracking technology to trace the intruder trajectory within a three-dimensional granular bed

[1]Beijing National Laboratory for Condensed Matter Physics and Laboratory of Soft Matter Physics, Institute of Physics, Beijing, 100190, China. [2]College of Physics and Electronic Engineering, Hainan Normal University, 571158, Haikou, China. [3]Technology and Engineering Center for Space Utilization, Chinese Academy of Sciences, Beijing, 100094, China. [4]School of Physical Sciences, University of Chinese Academy of Sciences, Beijing, 100049, China. [5]Songshan Lake Materials Laboratory, Dongguan, 523808, Guangdong, China. ✉e-mail: mayhou@iphy.ac.cn

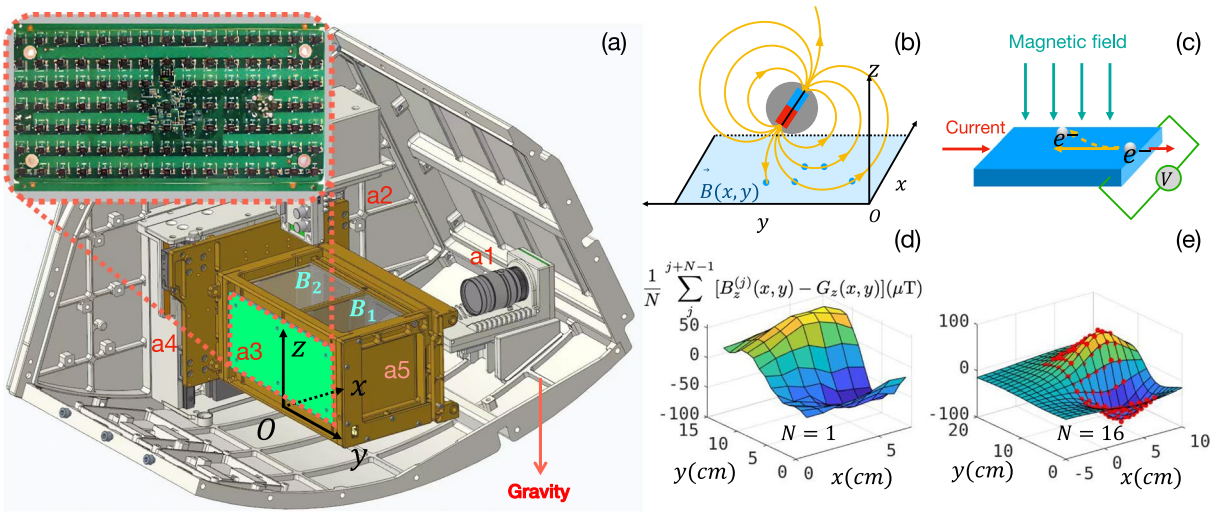

Fig. 1 (**a**) The experimental chamber on the CSS: (a1) and (a2) are the video cameras. (a3) is the Hall sensor array on *yOz* plane. (a4) is the linear motor, (a5) is the chamber, where B_1 and B_2 are the experiment containers. (**b**) the diagram of the Hall sensor array and the intruder. (**c**) the basic principle of Hall sensor. (**d**) the result after subtracting the background with the smoothing factor $N = 1$. (**e**) The red points for smoothing factor $N = 16$, and the surface is the fitting result with Eq. (3).

allow us to observe not only the initial and final states of the intruder but also the dynamical processes occurring during the interaction.

In this study, utilizing a magnetic particle tracking technique via two Hall-sensor arrays, we experimentally investigate the influence of gravity on intruder dynamics within a granular bed in reduced gravity provided by the centrifuge aboard the Chinese Space Station (CSS). This work has culminated in the creation of the first-of-its-kind dataset capturing the behavior of intruder scanning over parameter modes (f, A, g_{env}) with vibration frequencies f from 3 to 10 Hz and amplitudes A ranging from 0.5 to 6 mm under low gravity conditions, encompassing six gravity levels g_{env} ranging from $0.05g$ to $0.167g$ (lunar gravity). Our comprehensive dataset includes detailed three-dimensional positional coordinates of the intruder, its Euler angles, and the vibration waveform data.

Our analysis of the dataset reveals a competitive relationship between RBNE and BNE in low gravity environments[42]. The occurrence of these phenomena is governed by a critical vibration acceleration threshold: $\Gamma = 4\pi^2 A f^2 / g_{env}$, where Γ is the dimensionless vibration acceleration. The key findings are RBNE dominates when $\Gamma < \Gamma_c$; BNE prevails when $\Gamma > \Gamma_c$, and the critical value Γ_c is gravity related that it increases with decreasing gravity. Examining the correlation between the intruder's descent velocity and vibration parameters, we propose an impact-based granular segregation mechanism for RBNE. As gravity decreases, we observed reduced damping coefficient of bed particles and decreased hydrostatic pressure coefficient[42]. These observations suggest that under lower gravity conditions, bed particles are more susceptible to dispersion upon impact, facilitating deeper downward penetration of the intruder.

This research allows for comparison between Earth-based experiments and low-gravity condition, offers a unique perspective on the RBNE/BNE in reduced gravity environments, and enhances our comprehension of landing dynamics on asteroids, moons, and other low-gravity bodies. It aids in developing more accurate simulations for spacecraft-regolith interactions, and supports the development of technologies for processing and utilizing extraterrestrial materials.

By making this dataset publicly accessible, we aim to allow other researchers to verify our findings and build upon the results[42], to enable secondary analyses to maximize the scientific return.

Methods

Experimental apparatus. Our experimental apparatus is installed in the centrifuge of the CSS. The centrifuge generates gravity ranging from $0.1g$ to $2.0g$ where g is the gravitational acceleration of Earth. As shown in Fig. 1(a), the artificial gravity $g_{env} = \Omega^2 r$ is directed along the negative z-axis. The angular velocity $\vec{\Omega}$ of the centrifuge is along the negative direction of y-axis when the centrifuge rotates clockwise. The rotation radius r is 357 mm, which coincides with the center of the experimental chamber. A linear motor drives the container with sinusoidal vibrations in the z-direction, providing an amplitude of $A \leq 6$ mm. The frequency f (in Hz) can be any integer divisor of 600, such as 3,4,5,6,8 and 10 Hz. The experimental chamber is divided into two cubic containers, B_1 and B_2. Each container has a side length of 70 mm, with corners having a radius of 20 mm rounded off. The data discussed in this paper originates from the container B_1 shown in Fig. 1 (a).

The experimental container is filled with a granular bed to a thickness of 50 mm. The bed particles have diameters of 0.6–0.8 mm and a density of $2.5g/cm^3$. The container holds an intruder particle with a diameter of 10 mm and a density of $8.05g/cm^3$. To determine the position of the intruder, we embed a permanent magnet with a length of 5.7 mm inside it. The magnetic field generated by this magnetic dipole is detected by two Hall

sensor arrays located on the *xOy* and *yOz* planes. Figure 1(b) shows the schematic diagram of the magnetic field detected by Hall sensor array on *xOy* plane, which has 7 rows of sensors, with each row containing 15 sensors spaced 1 cm apart. The principle of Hall sensors is shown in Fig. 1(c), and each sensor measures the magnetic induction B in the (x, y, z) directions: $B_i^{(j)}(x, y)$, $i \in \{x, y, z\}$ and index j represents the frame number. The magnetic field resolution of the sensors is $0.15\,\mu$T in the horizontal directions and $0.25\,\mu$T in the vertical direction. The sensors sample data at a frequency of 30 frames per second, allowing the trajectory of the intruder particle to be reconstructed from the detected data. We use two sensor arrays A_1 and A_2 on the *yOz* and *xOy* planes respectively, as backups for each other, and their measurements can also be used for cross-validation. There are two video cameras, (a1) and (a2) monitoring the granular flow. The frame rate of the cameras is 60 fps, with a resolution of 1920×1080.

The acquirement of experimental data. At the start of each set of task, the centrifuge's rotational speed is first adjusted to generate the specified artificial gravity. After waiting for 60 seconds, the experimental apparatus receives the current task parameters uploaded from the ground station. Subsequently, the locking mechanism is disengaged, the linear motor and two cameras are powered on, and the motor moves from its initial position to the designated vibration center. A typical task usually consists of dozens of tests. There is a 30-second interval between each test, with durations of either 120 seconds or 240 seconds[43].

The algorithm for tracking the magnetic dipole. To illustrate the data processing steps, we use the Hall sensor array located on the plane as an example. Firstly, the raw data requires pre-processing. Each sensor located at position (x, y) (abbreviated from $(x, y, z=0)$) collects raw magnetic field $B_i^{(j)}(x, y)$ consisting of four components:

$$B_i^{(j)}(x, y) = C_i^{(j)} + G_i(x, y) + f_i^{(j)}(x, y) + \eta_i^{(j)} \tag{1}$$

The index i represents the components (x, y, z) of the magnetic field, and index j represents the frame number. To ensure the reliability of the experimental results, we choose the z-component of the magnetic field to determine the position of the intruder. The reason for this choice will be discussed later.

The first term on the right-hand side of Eq. (1) represents the geomagnetic field. Since all sensors share the common z-axis, the z-component of the geomagnetic field can be expressed as a constant $C_z^{(j)}$. The second term represents the background magnetic field inside the experimental apparatus, originating from instruments around the sensor array, such as the linear motor. The third term $f_z^{(j)}(x, y)$ represents the signal from the permanent magnet embedded in the intruder particle, which is a function of the magnet position (X, Y, Z) and its Euler angles (α, β). The fourth term $\eta_z^{(j)}$ represents the noise generated by the analog-to-digital converter.

In order to extract the pure dipole magnetic field $f_z^{(j)}(x, y)$ from the measured $B_z^{(j)}(x, y)$, we need to subtract the background term $G_z(x, y)$ from the raw data. The background magnetic field $G_z(x, y)$ can be measured by averaging the signals over M frames by removing the intruder particle:

$$G_z(x, y) = \frac{1}{M}\sum_{j=1}^{M} G_z^{(j)}(x, y). \tag{2}$$

In our experiment, $G_z(x, y)$ is collected on the ground, where M is fixed as 2000. It is important to note that $G_z(x, y)$ is influenced by the position of the linear motor, so we sample the motor positions at 1 mm intervals and record them in the background magnetic field data.

To reduce the noise $\eta_z^{(j)}$, we consider averaging the frames from the j-th to the $(j + N - 1)$-th in Eq. (1), where N can be referred to as the smoothing factor. Under the assumption that the intruder remains stationary over consecutive frames, the magnetic field data collected can be temporally averaged to mitigate noise. In quasi-static conditions, Eq. (1) can be reformulated as follows:

$$f_z^{(j)}(x, y) + C_z^{(j)} + \frac{1}{N}\sum_{j}^{j+N-1} \eta_z^{(j)} = \frac{1}{N}\sum_{j}^{j+N-1} B_z^{(j)}(x, y) - G_z(x, y). \tag{3}$$

The right-hand side terms of Eq. (4) can be experimentally determined, where the motor positions for B_z and G_z are identical. The results after subtracting the background magnetic field are shown in Fig. 1(d), which include the geomagnetic field $C_z^{(j)}$ and noise $\eta_z^{(j)}$. Under quasi-static conditions averaging over N frames, the noise term is significantly reduced as depicted in Fig. 1(e).

The 3D contour plots of f_x, f_y, and f_z are shown in Fig. 2(a–c), respectively. Specifically, f_x and f_y each exhibit two peaks and two valleys, while f_z displays only one peak and one valley. The complex contour patterns of f_x and f_y could lead to unreasonable experimental results. Therefore, we only consider the z-component of the magnetic field in our data processing, i.e., $i = z$.

The expression of $f_z^{(j)}(x, y)$ can be theoretically calculated. Given in our previous work[44], the terms $f_z^{(j)}(x, y) + C_z^{(j)}$ can be expressed as:

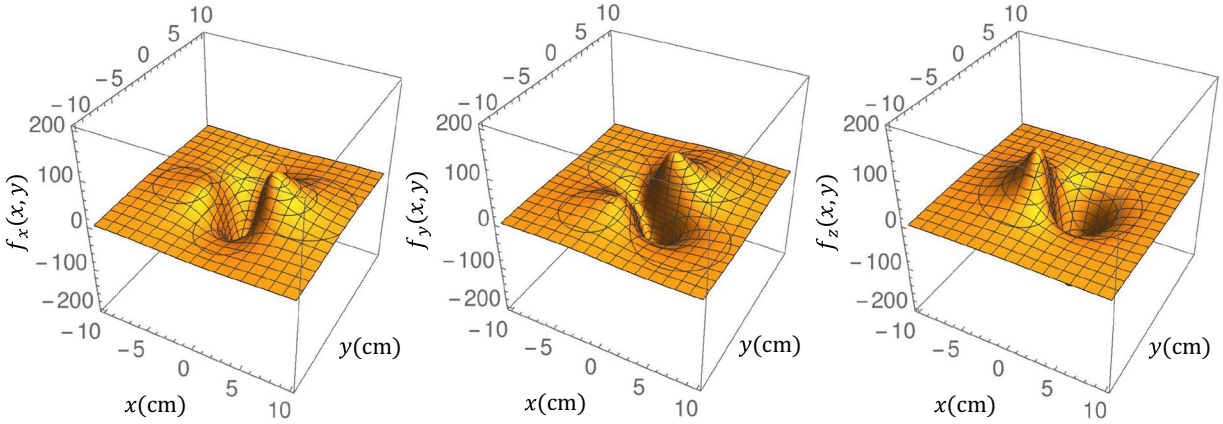

Fig. 2 An example of the magnet field generated by the intruder. The position of the intruder is ($X = Y = 0$, $Z = 3$ cm), and the Euler angle is $\alpha = \pi/4$, $\beta = \pi/3$.

$$f_z^{(j)}(x,y) + C_z^{(j)} = \frac{k(d\cos\alpha\cos\beta - Z)}{[(d\cos\alpha\cos\beta - Z)^2 + (-d\sin\beta - X + x)^2 + (-d\sin\alpha\cos\beta - Y + y)^2]^{3/2}} + \frac{k(d\cos\alpha\cos\beta + Z)}{[(d\cos\alpha\cos\beta + Z)^2 + (d\sin\beta - X + x)^2 + (d\sin\alpha\cos\beta - Y + y)^2]^{3/2}} + C_z^{(j)}. \quad (4)$$

the Euler angles (α, β) are defined as follows:

$$\begin{pmatrix} X_1 \\ Y_1 \\ Z_1 \end{pmatrix} = \begin{pmatrix} 1 & 0 & 0 \\ 0 & \cos(\alpha) & -\sin(\alpha) \\ 0 & \sin(\alpha) & \cos(\alpha) \end{pmatrix} \begin{pmatrix} \cos(\beta) & 0 & -\sin(\beta) \\ 0 & 1 & 0 \\ \sin(\beta) & 0 & \cos(\beta) \end{pmatrix} \begin{pmatrix} 0 \\ 0 \\ d \end{pmatrix} + \begin{pmatrix} X \\ Y \\ Z \end{pmatrix},$$
$$\begin{pmatrix} X_2 \\ Y_2 \\ Z_2 \end{pmatrix} = \begin{pmatrix} 1 & 0 & 0 \\ 0 & \cos(\alpha) & -\sin(\alpha) \\ 0 & \sin(\alpha) & \cos(\alpha) \end{pmatrix} \begin{pmatrix} \cos(\beta) & 0 & -\sin(\beta) \\ 0 & 1 & 0 \\ \sin(\beta) & 0 & \cos(\beta) \end{pmatrix} \begin{pmatrix} 0 \\ 0 \\ -d \end{pmatrix} + \begin{pmatrix} X \\ Y \\ Z \end{pmatrix} \quad (5)$$

where (X_1, Y_1, Z_1) and (X_2, Y_2, Z_2) are coordinates of the magnet poles. The half-length of the permanent magnet is $d = 2.85$ mm, and the magnetic dipole strength is $k = 2.77 \times 10^4 \mu\text{T} \cdot \text{cm}^2$. Since the sensor position (x, y) can have $7 \times 15 = 105$ values, which is much more than the number of unknowns $(X, Y, Z, \alpha, \beta, C_z)$, Eq. (3) forms an over-determined system. In MATLAB, we use initial values of $X = Y = Z = 0$ and $\alpha = \beta = 0$, $C_z = 0$, and fit the data using the Levenberg-Marquardt algorithm. In the example shown in Fig. 1(e), the fitted results agree well with the experimental measurements.

Data Records

Our experimental data is stored in the Zenodo repository. The DOI of this dataset[43] is 10.5281/zenodo.13622535. The raw magnetic field files under six low gravity conditions are stored in "/data_upload/magnet-syncdata/space/data/". In this directory, "mag_b1_*.dat" represents the data measured by A_1 array, and "mag_b2_*.dat" represents the data measured by A_2 array. The wildcard character "*" represents the task number. In each raw magnetic field data file, the first column indicates the position of the linear motor in millimeter. The second column contains numbers from 1 to 15, cycling to represent the row number on the sensor; every 15 rows constitute one frame. Columns 3 to 9 contain the B_x values, columns 11 to 17 contain the B_y values, and columns 19 to 25 contain the B_z values. The background magnetic field data measured on the ground is saved in "/data_upload/20220826_bias/".

Table 1 provides an overview for the tasks. To show the detailed information of each task, we include detailed parameter tables written in ".xlsx" files in the dataset. These files include the following items: starting and ending times of the vibration, frequency, amplitude, the dimensionless vibration acceleration $R = A\omega^2/g_{\text{env}}$, artificial gravity and the direction of rotation. These files are stored in "/data_upload/magnet-syncdata/space/tables/".

Technical Validation

To validate the reliability of the data, we plotted the fitting error as a function of Z coordinate, as shown in Fig. 3. When the intruder sinks to the bottom position of the container, $Z = 0.4$ cm. As Z increases, the signal-to-noise ratio of the magnetic field data decreases. This leads to an increase in fitting error. Comparing Fig. 3(a) and (b), increasing the smoothing factor N significantly reduces the fitting error. Figure 3(c) and (d) show the movement

Task number	Number of tests	Gravity/g	Rotation direction
66	48	0.05	CW
67	64	0.05	CW
68	40	0.05	CW
69	64	0.05	CW
70	32	0.05	CW
71	16	0.05	CW
72	20	0.05	CW
73	16	0.05	CW
74	28	0.05	CW
75	38	0.1	CW
76	5	0.1	CW
77	44	0.1	CW
78	33	0.1	CW
79	46	0.1	CW
80	24	0.167	CW
81	40	0.167	CW
83	24	0.167	CW
84	38	0.167	CW
85	32	0.1, 0.07	CW
86	48	0.07	CW
87	22	0.07	CW
88	51	0.07	CW
89	38	0.07, 0.1	CW
90	16	0.125	CW
91	77	0.125	CW
92	16	0.125	CW
93	46	0.125	CW
94	26	0.125	CW
95	48	0.15	CW
97	40	0.15	CW
98	31	0.15	CW
99	52	0.15	CCW
102	58	0.05	CW
104	24	0.05	CW
105	68	0.07	CW
106	60	0.1	CW
107	24	0.07	CW
108	8	0.07	CW
109	66	0.05	CW
111	68	0.07	CW
112	82	0.1	CW
113	73	0.125	CW
114	62	0.167	CW
115	78	0.15	CW
122	63	0.1, 0.125	CCW
124	23	0.1	CCW
125	24	0.1	CCW
126	17	0.1	CCW
127	42	0.15	CCW
128	40	0.167	CCW

Table 1. An overview for basic information of the tasks. The rotation direction CW for clockwise, CCW for counter-clockwise.

of the intruder at $g_{env} = 0.1\ g$, $f = 5$ Hz, $A = 3$ mm. Figure 3(c) is for $N = 1$ and Fig. 3(d) for $N = 8$. It can be observed that increasing the value of N does not affect the measurement results over long time scales, while the short-time motions are smoothed. In the provided processing program, N is an optional parameter for users. For situations with high signal-to-noise ratio of the measured magnetic field, we recommend using $N = 1$, while for

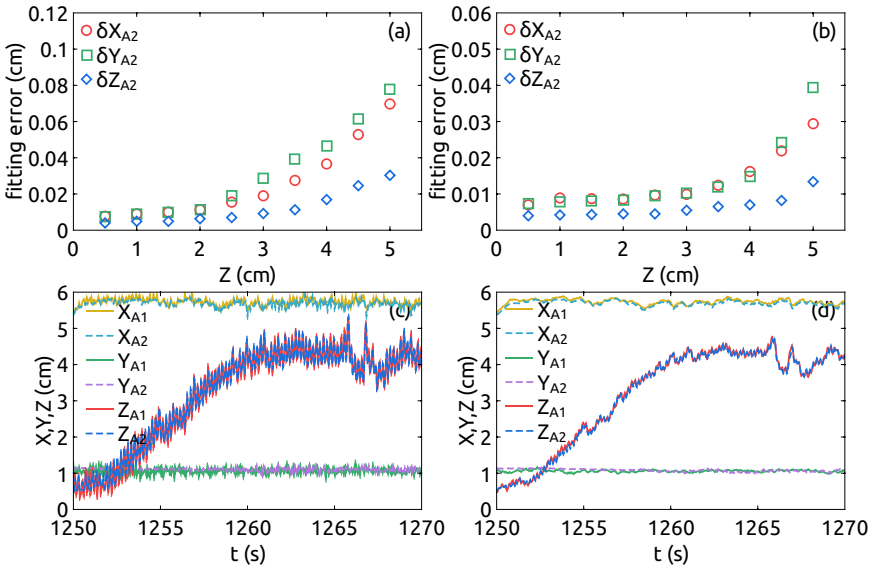

Fig. 3 Fitting errors of the measurement. (**a,b**) the fitting error as functions of Z (cm). (**a**) for N = 1, (**b**) for N = 8. In panels (**c**) and (**d**), positions (X_{A1}, Y_{A1}, Z_{A1}) are measured by A_1 and (X_{A2}, Y_{A2}, Z_{A2}) are measured by A_2. (**c**) for $N = 1$ and (**d**) for $N = 8$.

lower signal-to-noise ratios, a higher value of N is suggested. On the other hand, the results measured by the A_1 and A_2 sensor arrays, shown in Fig. 3(c) and (d), are consistent, demonstrating the high reliability of our data.

In reduced gravity conditions, the influence of the background magnetic field on the movement of the intruder particle is also estimated. The gradient of $G_z(x, y)$ within the experimental chamber may exert a force F on the magnetic dipole of the intruder particle. Under Earth's gravity, F is typically negligible. However, in a low-gravity environment, it is necessary to estimate the ratio of F to the gravitational force mg_{env} on the intruder particle. We take out the intruder particle and move the linear motor along the z-axis by a distance of 5.7 mm, which is equal to the length of the magnet. This allows us to measure the change in the background magnetic field around the xOy plane: $\Delta G_z = 0.115\ \mu$T. The magnetic force exerted on the intruder particle is:

$$|F_z| \leq \frac{\Delta G_z}{\mu_0} q_m \tag{6}$$

When the magnetic dipole is perpendicular to the xOy plane, $|F_z|$ reaches its maximum value. Here, μ_0 represents the vacuum permeability and $q_m = 4\pi k$ denotes the magnetic charge. At the bottom of the container, $|F_z| = 3 \times 10^{-6}$ N, which is significantly less than the gravitational force on the intruder particle under $0.1g$ ($mg_{\text{env}} = 4.11 \times 10^{-3}$ N). Therefore, the influence of the background magnetic field in the chamber on the motion of the intruder particle can be considered negligible.

Usage Note

We provide MATLAB code for processing the raw data. Users should run both "mag_alltest1.m" and "mag_alltest2.m" to process the data obtained from arrays A_1 and A_2, respectively. The variable "stacknumber" in both program codes corresponds to the smoothing factor N mentioned in this article, and can be adjusted as needed. At the start of the execution, MATLAB will print all the file names accompanied with a file number on the screen. Users can input a file number to process the magnetic data of the corresponding task. This execution may take several hours.

Once "mag_alltest1.m" and "mag_alltest2.m" have completed execution, text files prefixed with "trajectory_" will be generated in directory "/upload_data/magnet-syncdata/space/results/". In these output files, column 1 is the time in seconds, column 2 to column 4 are the coordinate (X, Y, Z). Column 5 and 6 are the Euler angles α and β. Column 7 records the position of the linear motor in millimeters, and column 8 is the geomagnetic field $C_z^{(j)}$. Columns 9–11 are the fitting error of (X, Y, Z).

We also provide a program code for visualizing the trajectories. To initiate the process, users should run "mag_information.m" to align the trajectories of the intruder particle measured by arrays A_1 and A_2. Users are also prompted to input the file number to process, as listed on the screen. The output files will be stored in "/upload_data/magnet-syncdata/space/results/" and prefixed with "align_". In these text files, the physical quantity of each column is consistent with those prefixed with "trajectory_". Next, users can execute "mag_makevideo.m"

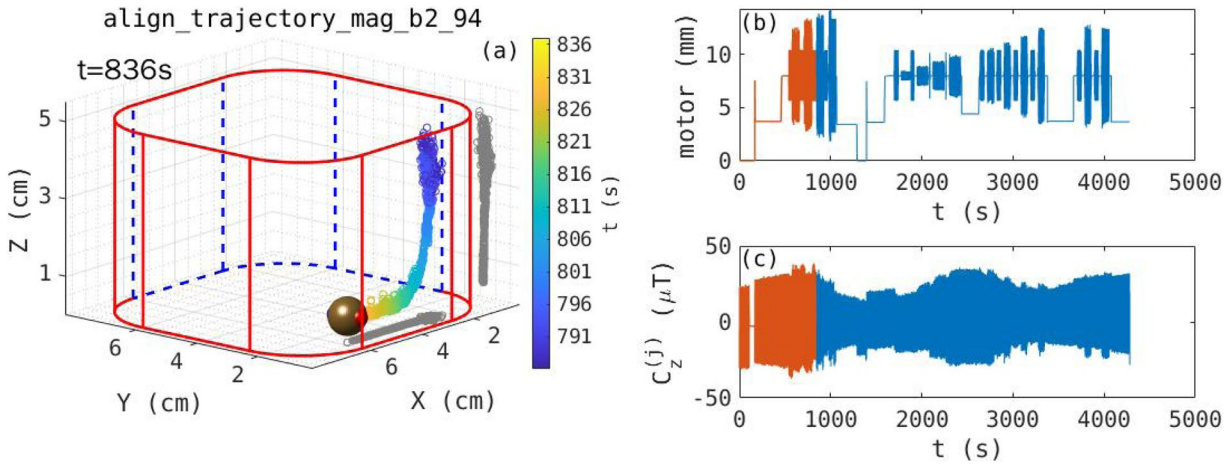

Fig. 4 A snapshot of the video of intruder motion. Panel (a) illustrates the framework of the container and the 3D trajectory of the intruder. The height of the framework is 50 mm, which is consistent with the filling height of the granular bed. The red and blue dots represents the direction of the internal magnetic dipole. Panel (b) plots the motor position as a function of time. Panel (c) is the geomagnetic field as a function of time. In (b) and (c), the red part of the curves show the passed time in the video.

to generate a video displaying the 3D trajectory of the intruder particle, as illustrated in Fig. 4. In this video, the poles of the magnet are plotted as red and blue dots on the intruder (see Fig. 4(a)). The red solid and blue dashed lines show the framework of the container. This video also provides the vibration amplitude (in millimeters) and geomagnetic field $C_z^{(j)}$ (in μT) as functions of time, as shown in Fig. 4(b) and (c). The generated video files are located in the "/upload_data/magnet-syncdata/space/videos/" directory.

Code availability

The code for processing this dataset requires MATLAB 2023a. GNU octave can be an alternative platform for executing this code, although it takes more time. The code files are located in the root directory of the uploaded data folder[43] (https://doi.org/10.5281/zenodo.13622535).

Received: 10 September 2024; Accepted: 23 January 2025;
Published online: 05 February 2025

References

1. Murdoch, N. *et al*. An experimental study of low-velocity impacts into granular material in reduced gravity. *Monthly Notices of the Royal Astronomical Society* **468**(2), 1259–1272 (2017).
2. Murdoch, N. *et al*. Low-velocity impacts into granular material: application to small-body landing. *Monthly Notices of the Royal Astronomical Society* **503**(3), 3460–3471 (2021).
3. Sunday, C. *et al*. The influence of gravity on granular impacts-i. a dem code performance comparison. *Astronomy & Astrophysics* **656**, A97 (2021).
4. Sunday, C. *et al*. The influence of gravity on granular impacts-ii. a gravity-scaled collision model for slow interactions. *Astronomy & Astrophysics* **658**, A118 (2022).
5. Joeris, K., Schönau, L., Keulen, M., Born, P. & Kollmer, J. E. The influence of interparticle cohesion on rebounding slow impacts on rubble pile asteroids. *npj Microgravity* **8**(1), 36 (2022).
6. Shinbrot, T., Sabuwala, T., Siu, T., Lazo, M. V. & Chakraborty, P. Size sorting on the rubble-pile asteroid itokawa. *Physical Review Letters* **118**, 111101 (2017).
7. Kudrolli, A. Size separation in vibrated granular matter. *Reports on Progress in Physics* **67**(3), 209 (2004).
8. Duran, J., Mazozi, T., Clément, E. & Rajchenbach, J. Size segregation in a two-dimensional sandpile: Convection and arching effects. *Physical Review E* **50**, 5138–5141 (Dec 1994).
9. Rosato, A., Strandburg, K. J., Prinz, F. & Swendsen, R. H. Why the brazil nuts are on top: Size segregation of particulate matter by shaking. *Physical Review Letters* **58**, 1038–1040 (1987). Mar.
10. Duran, J., Rajchenbach, J. & Clément, E. Arching effect model for particle size segregation. *Physical Review Letters* **70**, 2431–2434 (1993).
11. Knight, J. B., Jaeger, H. M. & Nagel, S. R. Vibration-induced size separation in granular media: The convection connection. *Physical Review Letters* **70**, 3728–3731 (1993).
12. Williams, J. C. The segregation of particulate materials. a review. *Powder Technology* **15**(2), 245–251 (1976).
13. Tancredi, G., Maciel, A., Heredia, L., Richeri, P. & Nesmachnow, S. Granular physics in low-gravity environments using discrete element method. *Monthly Notices of the Royal Astronomical Society* **420**(4), 3368–3380 (2012).
14. Matsumura, S., Richardson, D. C., Michel, P., Schwartz, S. R. & Ballouz, R.-L. The Brazil nut effect and its application to asteroids. *Monthly Notices of the Royal Astronomical Society* **443**(4), 3368–3380 (2014).
15. Maurel, C., Ballouz, R.-L., Richardson, D. C., Michel, P. & Schwartz, S. R. Numerical simulations of oscillation-driven regolith motion: Brazil-nut effect. *Monthly Notices of the Royal Astronomical Society* **464**(3), 2866–2881 (2016).
16. Chujo, T., Mori, O., Kawaguchi, J. & Yano, H. Categorization of brazil nut effect and its reverse under less-convective conditions for microgravity geology. *Monthly Notices of the Royal Astronomical Society* **474**(4), 4447–4459 (2018).

17. Bigot, J. *et al*. The bearing capacity of asteroid (65803) didymos estimated from boulder tracks. *Nature Communications* **15**(1), 6204 (2024).
18. Tancredi, G., Roland, S. & Bruzzone, S. Distribution of boulders and the gravity potential on asteroid itokawa. *Icarus* **247**, 279–290 (2015).
19. Noirhomme, M. *et al*. Particle dynamics at the onset of the granular gas-liquid transition. *Physical Review Letters* **126**, 128002 (2021).
20. Knight, J. B. *et al*. Experimental study of granular convection. *Physical Review E* **54**, 5726–5738 (1996).
21. Vanel, L., Rosato, A. D. & Dave, R. N. Rise-time regimes of a large sphere in vibrated bulk solids. *Physical Review Letters* **78**, 1255–1258 (1997).
22. Garcimartn, A., Maza, D., Ilquimiche, J. L. & Zuriguel, I. Convective motion in a vibrated granular layer. *Physical Review E* **65**, 031303 (2002).
23. Grossman, E. L. Effects of container geometry on granular convection. *Physical Review E* **56**, 3290–3300 (1997).
24. Hejmady, P., Bandyopadhyay, R., Sabhapandit, S. & Dhar, A. Scaling behavior in the convection-driven brazil nut effect. *Physical Review E* **86**, 050301 (2012).
25. Möbius, M. E. *et al*. Effect of air on granular size separation in a vibrated granular bed. *Physical Review E* **72**, 011304 (2005).
26. Windows-Yule, C. R. K., Weinhart, T., Parker, D. J. & Thornton, A. R. Influence of thermal convection on density segregation in a vibrated binary granular system. *Physical Review E* **89**, 022202 (2014).
27. Rosato, A., Prinz, F., Standburg, K. J. & Swendsen, R. Monte carlo simulation of particulate matter segregation. *Powder Technology* **49**(1), 59–69 (1986).
28. Schröter, M., Ulrich, S., Kreft, J., Swift, J. B. & Swinney, H. L. Mechanisms in the size segregation of a binary granular mixture. *Physical Review E* **74**, 011307 (2006).
29. Li, T., Cheng, K., Peng, Z., Yang, H. & Hou, M. Intruder trajectory tracking in a three-dimensional vibration-driven granular system: Unveiling the mechanism of the brazil nut effect. *Chinese Physics B* **32**(10), 104501 (2023).
30. Huerta, D. A., Sosa, V., Vargas, M. C. & Ruiz-Suárez, J. C. Archimedes' principle in fluidized granular systems. *Physical Review E* **72**, 031307 (2005).
31. Huerta, D. A. & Ruiz-Suárez, J. C. Vibration-induced granular segregation: A phenomenon driven by three mechanisms. *Physical Review Letters* **92**, 114301 (2004).
32. Oshtorjani, M. K., Meng, L. & Müller, C. R. Accurate buoyancy and drag force models to predict particle segregation in vibrofluidized beds. *Physical Review E* **103**, 062903 (2021).
33. Liu, C., Zhang, F., Wang, L. & Zhan, S. An investigation of forces on intruder in a granular material under vertical vibration. *Powder Technology* **247**, 14–18 (2013).
34. Yang, X.-qing, Zhou, K., Qiu, K. & Zhao, Y.-min Segregation of large granules from close-packed cluster of small granules due to buoyancy. *Physical Review E* **73**, 031305 (2006).
35. Nahmad-Molinari, Y., Canul-Chay, G. & Ruiz-Suárez, J. C. Inertia in the brazil nut problem. *Physical Review E* **68**, 041301 (2003).
36. Shinbrot, T. & Muzzio, F. J. Reverse buoyancy in shaken granular beds. *Physical Review Letters* **81**, 4365–4368 (1998).
37. Hong, D. C., Quinn, P. V. & Luding, S. Reverse brazil nut problem: Competition between percolation and condensation. *Physical Review Letters* **86**, 3423–3426 (2001).
38. Balista, J. A. F. & Saloma, C. Modified inelastic bouncing ball model of the brazil nut effect and its reverse. *Granular Matter* **20**, 1–12 (2018).
39. Jenkins, J. T. & Yoon, D. K. Segregation in binary mixtures under gravity. *Physical Review Letters* **88**, 194301 (2002).
40. Breu, A. P. J., Ensner, H.-M., Kruelle, C. A. & Rehberg, I. Reversing the brazil-nut effect: Competition between percolation and condensation. *Physical Review Letters* **90**, 014302 (2003).
41. Güttler, C., Borstel, Ivon, Schräpler, R. & Blum, J. Granular convection and the brazil nut effect in reduced gravity. *Physical Review E* **87**, 044201 (2013).
42. Cheng, K. *et al*. Unraveling the role of gravity in shaping intruder dynamics within vibrated granular media. *Communications Physics* **7**(1), 425 (2024).
43. K. Cheng et al. Three dimensional trajectories of a magnetic sphere in a shaken granular bed under low gravity, *Zenodo*. https://doi.org/10.5281/zenodo.13622535 (2024).
44. Cheng, K. *et al*. Tracking the motion of an intruder particle in a three-dimensional granular bed on-board the chinese space station. *Microgravity Science and Technology* **36**(2), 1–8 (2024).

Acknowledgements

We thank for the support by the ESA-CMSA/CSU Space Science and Utilization collaboration program, the Space Application System of China Manned Space Program YYWT-0601-EXP-20, and the National Key R&D Program of China (2022YFF0503504). Ke Cheng and Tuo Li would like to thank the support by Wenzhou Institute, University of Chinese Academy of Sciences. Special thanks to China Manned Space Engineering and Technology and Engineering Center for Space Utilization of Chinese Academy of Sciences for providing scientific data for this study.

Author contributions

Ke Cheng conducted the data analysis. Meiying Hou wrote the manuscript and is responsible for the research. Wei Sun, Zhihong Qiao, and Xiang Li are responsible for the instrumentation. Tuo Li and Mingcheng Yang participate in the discussion.

Competing interests

The authors declare no competing interests.

Additional information

Correspondence and requests for materials should be addressed to M.H.